THE JOURNAL OF PHYSICAL CHEMISTRY C

Article

Cite This: J. Phys. Chem. C XXXX, XXX, XXX−XXX

pubs.acs.org/JPCC

Cu-Based Single-Atom Catalysts Boost Electroreduction of CO_2 to CH_3OH: First-Principles Predictions

Zhonglong Zhao and Gang Lu*

Department of Physics and Astronomy, California State University Northridge, Northridge, California 91330, United States

Supporting Information

ABSTRACT: Electrochemical CO_2 reduction reaction (CO_2RR) to fuels represents one of the most attractive approaches to mitigate our pressing energy and environmental threats. Cu is the best known metal catalyst that can produce an appreciable amount of hydrocarbons from CO_2, but it suffers from a high overpotential and poor selectivity. In this work, by means of first-principles calculations, we predict that Cu-based single-atom alloys (SAAs) could be exceptional electrocatalysts for CO_2RR. In particular, we predict that Co@Cu SAA could be a promising catalyst on which methanol can be produced at a low overpotential and high selectivity. The isolated Co atoms lead to a narrowed d-band and an upshifted d-band center which can stabilize chemisorbed CO_2 on a surface, significantly lowering the reaction barrier. The narrowed Co d-band increases the bonding to a key intermediate, which in turn eliminates the need for its migration and enables a selective and efficient production of CH_3OH through the pathway of $CO_2 \rightarrow COOH^* \rightarrow CO^* \rightarrow COH^* \rightarrow CHOH^* \rightarrow CH_2OH^* \rightarrow CH_3OH$.

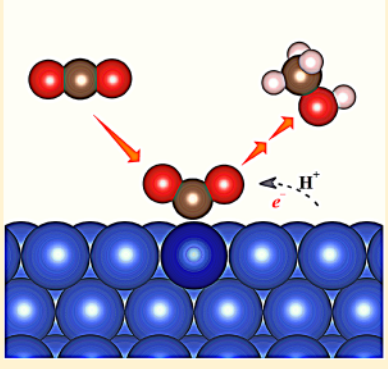

1. INTRODUCTION

The electroreduction of CO_2 into chemical feedstocks with renewable energy sources, such as solar, hydro, and wind, represents a promising route to mitigate our dependence on fossil fuels and to remediate environmental threats.[1−3] Elemental metals, including Cu, Au, Ag, Pt, and Ni, have been explored as electrocatalysts for CO_2RR.[4−9] However, they all suffer from problems such as sluggish kinetics, low efficiency, and poor selectivity. For example, although Cu can catalyze the formation of hydrocarbons, including methane (CH_4) and ethylene (C_2H_4),[4] it does so with a high overpotential (~1 V) and a large number of byproducts.[5−7] To overcome these problems, innovative strategies have been proposed. First strategy is to tap into metallic nanocatalysts,[10] such as Cu nanoparticles (NPs) and nanowires, which are shown to exhibit much enhanced catalytic activities for CO_2RR.[11−15] Design of metal alloys, such as near-surface alloys (NSA) and core/shell NPs, represents another strategy to improve the efficiency and selectivity of CO_2RR.[16−21] For instance, Cu−Au bimetallic NPs have demonstrated enhanced activities for CO production,[17] while Cu−Ag NSAs are revealed to be selective for multicarbon carbonyl-containing products.[18] More recently, single-atom catalysts (SACs) with metal atoms dispersed onto porous carbon materials or metal oxides are discovered to be highly active for CO_2RR;[22−25] they are shown to display maximum atomic efficiencies and excellent selectivity thanks to their unique electronic properties.[26]

As a special class of SACs, single-atom alloys (SAAs) consist of single solute atoms of an active metal dispersed onto the surface of a noble metal matrix.[27−34] Owing to the metallic bonds between the solute and the host, the active solute atoms in SAAs are expected to be more stable against phase separations compared to other SACs.[35] Some unique and desirable features have emerged in SAAs, which can be attributed to low concentrations of the solute atoms (1−10%).[29,36−39] Among them is the synergistic catalysis rendered by the cooperation between the solute and the host.[40] For example, in Pd−Cu and Pt−Cu SAAs, it was found that low-temperature H_2 dissociation could occur facilely on the single-atom sites (Pd and Pt), followed by a spillover of atomic H to the nearby Cu host, where selective hydrogenation takes place.[27,28] Another interesting feature has to do with electronic structures of SAAs, which deviate significantly from a linear interpolation of the constituent electronic structures.[41] A recent study has shown that the d-band of the solute Cu atoms in the Ag host becomes atomically narrow, leading to π bonding to the adsorbed oxygen. As a result, the overall binding strength is increased compared to that on the bulk Cu surface.[42]

It is known that as the initial step of CO_2RR, the capturing of CO_2 is of critical importance to the subsequent reactions. However, CO_2 is highly inert and its fixation is often thermodynamically unfavorable under ambient conditions.[43] For example, CO_2 is found to interact weakly with the Cu surface by forming a linear and physisorbed configuration (l-CO_2),[44] which results in a high energy barrier for the initial hydrogenation.[45,46] On the other hand, bent and chemisorbed configurations (b-CO_2) can be formed on other metal surfaces.[47,48] In particular, a bent b-CO_2 configuration has

Received: December 26, 2018
Revised: January 28, 2019
Published: January 30, 2019

DOI: 10.1021/acs.jpcc.8b12449
J. Phys. Chem. C XXXX, XXX, XXX−XXX

been identified as a crucial transition state (TS) in the electroreduction of l-CO_2 on the Cu(111) surface.[45,46] Although b-CO_2 configurations are energetically less stable than l-CO_2 on Cu(111), b-CO_2 could actually bond more strongly to the surface if formed. Hence, we hypothesize that if b-CO_2 could be stabilized on the Cu surface, it may lower the activation energies for the initial hydrogenation steps. Because SAAs can modulate the adsorption strength,[42] we aim to uncover Cu-based SAAs on which b-CO_2 becomes stable, which in turn may lead to more efficient and selective CO_2RR.

According to the d-band theory, a change in the bandwidth shifts the d-band center, which in turn affects the coupling of molecular orbitals to the d states.[49] Therefore, an atomically narrow d-band in the SAA may result in a drastic shift of the d-band center, which leads to a significant change to the adsorption energy compared to traditional alloys, and provides an effective means to stabilize b-CO_2. Motivated by a recent study which computationally screened SAAs for enhanced catalytic activities,[50] we aim to discover Cu-based SAAs as superior catalysts for CO_2RR. More specifically, we search for SAAs that can stabilize b-CO_2 via first-principles density functional theory (DFT) calculations. It is important to note that the stabilization of b-CO_2 only ensures facile reaction of the initial hydrogenation step in CO_2RR (which contributes to the formation of CO and formic acid). Thus, we have to subject the screened SAAs to subsequent reaction steps, particularly the overpotential-determining hydrogenation step. To this end, we have examined a dozen of reaction intermediates in determining the lowest overpotential reaction pathway that reduces b-CO_2 to CH_3OH. A particular attention is paid to CO_2 because the initial hydrogenation step is relevant to all CO_2RR catalysts, regardless of the final products. Because the hydrogen evolution reaction (HER) is an undesirable side reaction that competes with CO_2RR, we also examine HER on the proposed catalysts. By means of extensive DFT calculations, we have identified a promising SAA catalyst, Co@Cu, which can reduce b-CO_2 to liquid fuel CH_3OH with a low overpotential and high selectivity. We hope that this work could inspire experimental effort to corroborate our findings and open doors to further study of SAAs as electrocatalysts.

2. COMPUTATIONAL DETAILS

2.1. Electronic Structure Calculations. Cu(111)-based SAAs were modeled by a four atomic layer and a 3 × 3 in-plane supercell. One Cu surface atom was replaced by a metal dopant atom M (M = Ti, V, Cr, Mn, Fe, Co, Ni, Zn, Zr, Nb, Mo, Tc, Ru, Rh, Pd, Ag, Cd, Hf, Ta, W, Re, Os, Ir, Pt, Au, Hg), which is considered as the single solute atom in SAAs. The surface solute concentration is ∼10%, which is similar to the experimental concentrations of SAAs at a higher end.[29] The adjacent computational slabs were separated by a 15 Å vacuum in the normal direction of the surface. The bottom two Cu layers were fixed while the top two layers were allowed to fully relax. DFT calculations were performed using the Vienna ab initio simulation package.[51] The exchange−correlation interaction was described by Perdew−Burke−Ernzerhof (PBE) functional.[52] The PBE/DFT-D3 scheme[53] with explicit dispersion corrections was also used for weak adsorbates. Heyd−Scuseria−Ernzerhof hybrid functional[54−56] was employed in the electronic density of states calculations. The plane-wave energy cutoff was 400 eV and the Brillouin-zone was sampled with a 3 × 3 × 1 *k*-mesh according to the Monkhorst−Pack scheme.[57] All atomic structures were optimized until the forces were less than 0.03 eV Å^{-1}. Spin-polarized calculations were performed for SAAs in the presence of magnetic solutes, such as Cr, Mn, Fe, Co, and Ni. All energy barrier calculations were performed using the climbing-image-nudged elastic band method.[58] The TSs were determined with 6 to 10 images and confirmed with the frequency analysis.

2.2. Free Energy Calculations. The computational hydrogen electrode (CHE) model was used to calculate the reaction free energy for the elementary steps of CO_2RR.[59] In the CHE model, the chemical potential of a proton−electron pair is defined in equilibrium with half of that of gaseous H_2 at 0 V, 10 1325 Pa, any pH values, and temperatures on a relative hydrogen electrode (RHE) scale. The chemical potential was then shifted by $-eU$ (e is the elementary positive charge) when an external potential U was applied. The potential-dependent reaction free energy for an elementary step A* → AH* (* indicates adsorbed species) is thus defined as follows

$$\Delta G = G(\mathrm{AH}^*) - G(\mathrm{A}^*) - [1/2G(\mathrm{H}_2) - eU] \quad (1)$$

Zero-point energies (ZPEs), heat capacities, and entropies were calculated based on the molecular vibration analysis[60] and used to convert the electronic energies into free energies at 298 K.

2.3. Activation Barrier Calculations. We followed the work of Nie et al.[45,46] in estimating the activation energy barriers. More specifically, the activation barrier for an elementary electrochemical reaction ($A^* + H^+ + e^- \rightarrow AH^*$) can be derived from the analogous (DFT-accessible) hydrogenation reaction ($A^* + H^* \rightarrow AH^*$).[45,46] This is rationalized by the assumption that the former is an inner-sphere reaction and the TS is reached when the proton arrives at the adsorbed species, A*. The electron transfer is considered ultrafast once the proton attains the TS. However, this assumption does not imply that surface H* species must be formed as a precursor. The activation barrier (E_{act}) as a function of the electrode potential U is thus calculated as

$$E_{act}(U) = E_{act}{}^0(U^0) + \beta'(U - U^0) \quad (2)$$

where E^0_{act} is the barrier computed from DFT and the ZPE correction. U_0 is the equilibrium potential for the reductive adsorption of the proton, at which the chemical potential of the adsorbed H* is equal to that of a proton−electron pair ($H^+ + e^-$). β' is an effective symmetry factor defined as

$$\beta' = \beta + (\mu_{TS} - \mu_{reactant})/d \quad (3)$$

β is taken as 0.5 for all reaction steps. The second and correction term includes the variation in the surface dipole moments between the reactant and TS. d is the distance for the counter charge to approach the electrode surface in the Helmholtz model and is assumed to be 3 Å. More details about the activation barrier calculations can be found elsewhere.[45,46] The maximum barrier over which a reaction is presumed to occur at room temperature is set as 0.4 eV.[45,46,61]

2.4. Water-Assisted Reaction Models. In both free energy and activation barrier calculations, we have considered the presence of water molecules in assisting the hydrogenation steps. More specifically, water can assist the reactions in two different manners, which are referred to as the water-solvated (WS) model and H-shuttling (HS) model in literature.[45,46] To hydrogenate an atom that is directly bonded to the surface, the WS model is applied. In this case, a surface proton is transferred directly to the atom and is assisted by the hydrogen bonds between the water molecule and the adsorbate. Note that

DOI: 10.1021/acs.jpcc.8b12449
J. Phys. Chem. C XXXX, XXX, XXX−XXX

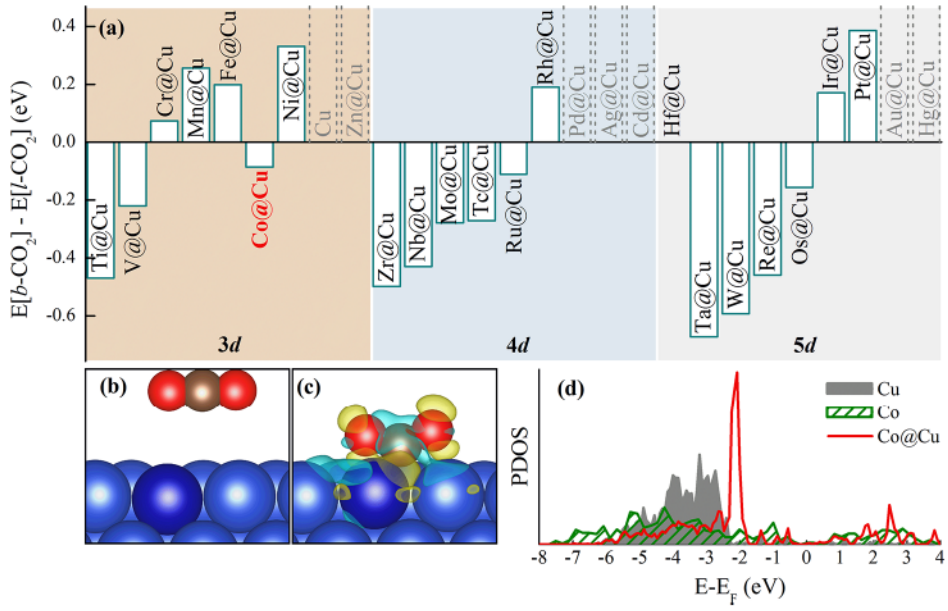

Figure 1. (a) Energy difference between b-CO_2 and l-CO_2 adsorption on the considered SAAs. Dashed columns indicate the SAA surfaces on which b-CO_2 transfers to l-CO_2 spontaneously upon the geometric optimization. The adsorption structure and differential charge density isosurfaces for (b) l-CO_2 and (c) b-CO_2 on Co@Cu. Cyan and yellow isosurfaces correspond to the charge density contour of −0.01 and +0.01 e Å^{-3}. Blue, dark blue, gray, and red spheres represent Cu, Co, C, and O atoms, respectively. Note that the differential charge density is too small to be visible in (b). (d) The projected density of states (PDOS) of the d-band for the Co atoms on Co@Cu as compared with that of Cu and Co atoms on Cu(111) and Co(111) surfaces, respectively.

the C atom of the adsorbates in CO_2RR often bonds directly to the surface, thus the WS model is applicable to its hydrogenation in forming the C−H bond. On the other hand, to hydrogenate an atom that is indirectly bonded to the surface (such as the O atom), the HS model is more appropriate. In this case, the surface proton is transferred to the water molecule, which concurrently shuttles another proton to the adsorbate, analogous to the Grotthuss mechanism. In other words, the water molecule assists the reaction by shortening the proton migration distance. The HS model is thus more suitable for the formation of the O−H bond.[45,46] In this work, only one model is assumed to operate in each reaction step, and specified in the following discussion. The WS and HS models have been used to estimate the activation barriers and kinetics of CO_2RR on Cu surfaces, which are consistent with experimental results.[45,46,61]

3. RESULTS AND DISCUSSION

3.1. l-CO_2 Versus b-CO_2. It is known that CO_2 binds weakly to the Cu(111) surface via the linear (l-CO_2) configuration and the bent b-CO_2 configurations are not stable on the Cu(111) surface.[44] In fact, all bent CO_2 structures with various bending angles relaxed to the l-CO_2 structure in our DFT calculations. We next examine whether b-CO_2 could be stabilized on Cu-based SAAs by incorporating 26 metal solutes to the Cu(111) surface. Figure 1a shows the energy difference between b-CO_2 and l-CO_2 on the 26 SAAs. We find that b-CO_2 can be stabilized on SAAs with metal solutes, such as Ti, V, Co, Zr, Nb, Mo, Tc, Ru, Ta, W, Re, and Os, for which the energy difference is negative. In Figure 1b,c, we display the differential charge density of l-CO_2 and b-CO_2 on the Co@Cu SAA surface, respectively. The positive (negative) value of the differential charge density indicates charge accumulation (deficit) when CO_2 is adsorbed onto the surface. Compared to l-CO_2, b-CO_2 is closer to the surface, and both C and O atoms in b-CO_2 are bonded to the metal atoms. In contrast, the bonding between l-CO_2 and the surface is too weak to be visible in Figure 1b. We find that the ranking in the relative stability between l-CO_2 and b-CO_2 follows roughly that in the electronegativity, that is, the less electronegative of the metal solute, the more stable of b-CO_2 on the surface.

Among the SAAs that stabilize b-CO_2, Co@Cu is the most promising catalyst for CO_2RR for two reasons. First, the binding of the relevant intermediates (such as CO_2) on Co@Cu is not overly strong, thus their desorption is facile for following reactions. We hypothesize that strong binding of b-CO_2 would lead to overbinding of the intermediates and the products on the same surface. To test this hypothesis, we take Zr@Cu as an example of the SAAs on which b-CO_2 is most stabilized (Figure 1a). We find that the desorption energy of CH_3OH on Co@Cu is ∼0.3 eV, much smaller than that (∼1 eV) on Zr@Cu. Moreover, the activation barrier for the hydrogenation of b-CO_2 to COOH* (discussed below) on Zr@Cu is 0.80 eV, more than twice that (0.36 eV) on Co@Cu. Second, it has been demonstrated experimentally that single Co atoms can be introduced and stabilized on Cu(100) surfaces.[62,63] Therefore, Co@Cu is likely to be synthesized experimentally. On the other hand, although other SAAs (such as V@Cu, Ru@Cu, and Os@Cu) exhibit similar favorable binding stabilities to b-CO_2 (Figure 1a), it is less clear whether they can be synthesized experimentally.

Recognizing the importance of stability, we have examined the stability of isolated Co atoms on the Cu(111) surface by DFT calculations. As Co atoms could potentially aggregate to form islands on the Cu surface or they could diffuse into the interior of Cu, the following calculations are performed to address the two possibilities. To check the tendency of aggregation, we construct a 4 × 4 in-plane supercell with two Co atoms on the surface, and calculate the migration barrier for the Co atoms forming a dimer along the *a*-axis (from Co1 to Cu2 in Figure S1). We find that the aggregation of Co atoms on the Cu(111) surface is

DOI: 10.1021/acs.jpcc.8b12449
J. Phys. Chem. C XXXX, XXX, XXX−XXX

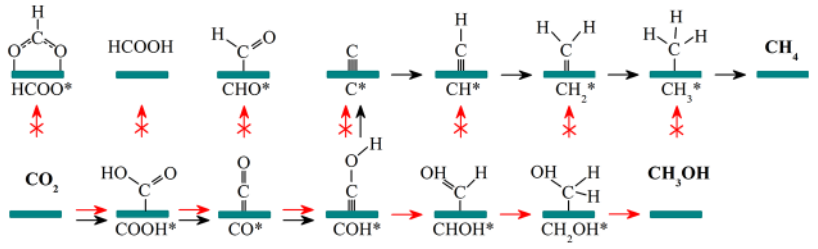

Figure 2. Reaction pathway for CO_2RR to CH_3OH on Co@Cu (red arrows) established in this work and to CH_4 on Cu(111) (black arrows) established by Nie et al.[45,46] The branches examined in this work are indicated by red arrows with crosses. $H^+ + e^-$ reactants and H_2O are omitted for clarity.

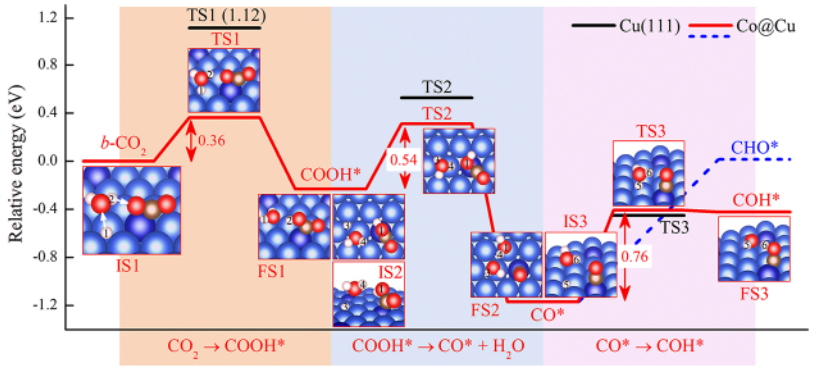

Figure 3. Relative energy diagram for the reduction of b-CO_2 to COH* on Co@Cu under zero voltage. The free energy change between the initial and final state is calculated via eq 1, while the activation barrier (i.e., energy difference between the initial and TSs) is calculated via eq 2. The optimized atomic geometries of the initial states (IS1, IS2, and IS3), TSs (TS1, TS2, and TS3), and final states (FS1, FS2, and FS3) are shown in the insets. Note that two different views are presented for IS2. Blue, dark blue, gray, red, and white spheres represent Cu, Co, C, O, and H atoms, respectively. Key atoms are numbered to facilitate the discussion. The energy barriers for the corresponding TSs on Cu(111) (black bars) are taken from previous works.[45,46]

endothermic by 0.15 eV and the migration barrier is as high as 2.05 eV, which is too high to be overcome at normal electrochemical conditions. Note that because of the symmetry of the surface, our conclusion is also valid along the *b*-axis and the diagonal *ab* axis. To access the possibility of Co diffusion into Cu, we calculate the energy barrier of a Co atom diffusing from the surface to the subsurface (from Co to Cu2 in Figure S2). The diffusion barrier is found to be 1.93 eV, which renders the diffusion highly unlikely. Although the presence of surface Cu vacancies adjacent to Co may facilitate aggregation and diffusion, the Cu vacancy formation energy adjacent to Co is calculated as 0.53 eV, which is very high. Once the vacancy is formed, the energy barrier for aggregation and diffusion is 0.90 and 0.61 eV, respectively, giving rise to a total energy cost of 1.43 and 1.14 eV for each process. Therefore, we conclude that Co segregation to form islands on the Cu(111) surface or its diffusion into Cu interior is unlikely to happen, which echoes the experimental observations that single Co atoms can be stabilized on Cu(100) surfaces.[62,63] Finally, because the lattice mismatch between Co and Cu is small (~2%), the SAA once formed is likely to be stable against surface reconstructions.

In the remaining part of the paper, we will focus on Co@Cu SAA. To further ascertain the stability of b-CO_2 over l-CO_2 on Co@Cu, we have calculated the free energy difference between the two configurations using the PBE-D3 functional. We find that b-CO_2 remains more stable than l-CO_2 on Co@Cu with 0.21 eV difference in free energy. Because the presence of water on the surface may impede the adsorption of CO_2, we have also calculated the free energy for the following surface configurations by incorporating water molecules onto the surface (one water molecule in each supercell): (1) b-CO_2 on the Co site and H_2O on the adjacent Cu site, (2) l-CO_2 on the Co site and H_2O on the adjacent Cu site, (3) H_2O on the Co site and l-CO_2 on the adjacent Cu site, and (4) H_2O on the Co site and b-CO_2 on the adjacent Cu site (Figure S3). We find that the configuration (1) has the lowest free energy, thus it is most stable. The results suggest that b-CO_2 is more stable than l-CO_2 on the Co@Cu surface even in the presence of water molecules.

Figure 1d shows the PDOS of the Co atom (red) in Co@Cu along with the PDOS of a Cu atom (gray) and of a Co atom (green) in the corresponding pure surfaces. The most prominent feature in the PDOS for Co@Cu is the appearance of a free atom-like d-band centered at −2.1 eV, in a sharp contrast to the broader d-bands of the pure metals. For transition metals whose d bands are more than half-filled (such as Co), the rigid band model suggests that the band narrowing would shift the d-band center up,[49] and this shift is particularly striking for the free atom-like d-band. As shown in Figure 1d, the Co d-band center in Co@Cu is shifted 1.14 eV higher (more positive in energy) relative to the pure Co surface. The well-known d-band model predicts that an upshift of the d-band center yields stronger bonding to the adsorbates,[49] which is clearly evident in Figure 1. The Bader charge analysis indicates that there is significant charge transfer from the metal to b-CO_2, forming an activated $CO_2^{\delta-}$ radical anion (the charges on b-CO_2 and l-CO_2 are calculated as 0.59 e and 0.03 e, respectively).

3.2. Reaction Pathway on Co@Cu. In the following, we will discuss in detail the reaction pathway from b-CO_2 to CH_3OH on Co@Cu. All plausible pathways, including those identified on Cu, are examined.[6,45,46] In particular, the reduction

DOI: 10.1021/acs.jpcc.8b12449
J. Phys. Chem. C XXXX, XXX, XXX−XXX

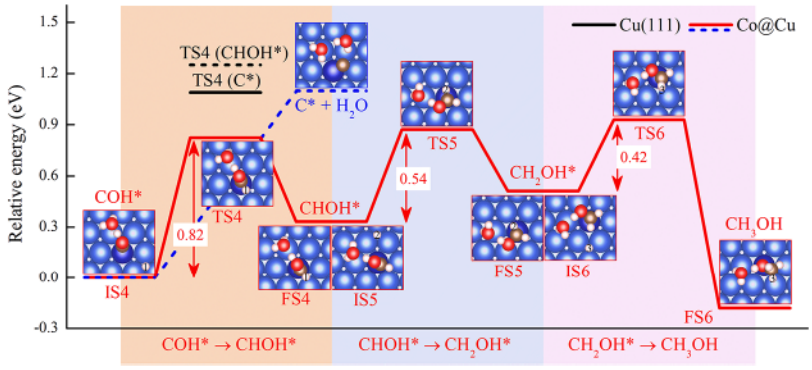

Figure 4. Relative energy diagram for the reduction of COH* to CH_3OH on Co@Cu under zero voltage. The free energy change between the initial and final state is calculated via eq 1, while the activation barrier (i.e., energy difference between the initial and TSs) is calculated via eq 2. The optimized atomic geometries of the initial states (IS4, IS5, and IS6), TSs (TS4, TS5, and TS6), and final states (FS4, FS5, and FS6) are shown in the insets. Blue, dark blue, gray, red, and white spheres represent Cu, Co, C, O, and H atoms, respectively. The energy barriers for the corresponding TSs on Cu(111) are taken from previous works.[45,46]

of CO_2 into formic acid (HCOOH), carbon monoxide (CO), and methane (CH_4) is considered. As shown in Figure 2, the established pathway: $CO_2 \rightarrow COOH^* \rightarrow CO^* \rightarrow COH^* \rightarrow CHOH^* \rightarrow CH_2OH^* \rightarrow CH_3OH$ coincides partially with that for the formation of CH_4 on Cu(111)[45,46] but deviates from it at the reduction step of COH*. COH* is reduced to CHOH* on Co@Cu but to C* on Cu. The origin of this deviation is discussed below. Note that along the pathway, the first three steps ($CO_2 \rightarrow COOH^* \rightarrow CO^* \rightarrow COH^*$) proceed via the HS model, while the remaining steps involve the WS model. Because each Co atom can accommodate only one C-based intermediate, and the Co atoms are well separated in SAAs, the C−C coupling between the intermediates is too weak to form C_2 hydrocarbons,[40] which underlies the higher selectivity of SAAs.

3.3. $CO_2 \rightarrow COOH^*$. It is well known that the proton transfer to weakly bound l-CO_2 on Cu(111) is energetically costly, and the activation barrier for its hydrogenation to COOH* is between 0.73 and 1.65 eV.[45,46] Remarkably, on Co@Cu, the activation barrier of b-CO_2 to COOH* is reduced to 0.36 eV (Figure 3), a dramatic decrease compared to Cu(111). The initial hydrogenation step is found to be exothermic (0.23 eV) on Co@Cu. As shown in Figure 3, the reduction (IS1 → TS1 → FS1) takes place via a simultaneous proton transfer from the surface to H_2O and from H_2O to the O atom of CO_2 (the two protons are labeled as 1 and 2 in the insets of Figure 3). The bond angle of CO_2 in the TS TS1 (134.83°) is close to that in the initial state IS1 (138.93°), rendering a low energy barrier. A branched pathway from b-CO_2 to HCOO* (Figure 2) via the WS model has a higher energy barrier of 0.66 eV because of a strong interaction between the C atom and Co (Figure S4).

3.4. COOH* → CO*. The reduction of COOH* to CO* (and H_2O) on Co@Cu follows closely to that on Cu(111). The activation barrier for this step on Co@Cu is 0.54 eV, which is 0.22 eV lower than that on Cu and the reaction is again exothermic (0.94 eV). During the proton−electron transfer process (IS2 → TS2 → FS2), the formation of the O−H bond (H4 and O1 in the insets of Figure 3) is accompanied by the breaking of the C−OH bond, spilling out a water molecule. We find that in contrast to Cu, COOH* cannot be reduced to HCOOH on Co@Cu (Figure S5). This is due to the fact that C in COOH* interacts more strongly with Co, owing to its narrowed d-band, than with the pure Cu surface. Thus, the narrowed d-band in Co@Cu contributes to its selectivity toward the final product.

3.5. CO* → COH*. CO* can be reduced to CHO* or COH* as shown in Figure 2. However, the reduction of CO* to CHO* on Co@Cu is highly endothermic, with 1.19 eV increase in free energy. In contrast, the free energy increase is 0.75 eV for the reduction of CO* to COH*. Hence, COH* is much more likely to be formed on Co@Cu, with an activation barrier of 0.76 eV (Figure 3). Although on the Cu surface COH* is also more stable than CHO*, its energy difference is only 0.03 eV.[45,46] Finally, we find that CO bonds very strongly to Co@Cu (the desorption energy is calculated as 2.25 eV). Thus CO is not a viable product on Co@Cu, in contrast to Cu. Because the PBE functional was reported to overestimate CO desorption energy,[64] we also calculated the CO desorption energy by using the revised PBE functional,[65] which yielded a value of 1.92 eV. Because this is still a very large energy, our conclusion remains the same, that is, CO is not a viable product on Cu@Cu.

3.6. COH* → CHOH*. As mentioned above, the reaction pathway on Co@Cu deviates from that on Cu(111) at the reduction step of COH*. On Cu(111), the reactant COH* occupies the hollow site while the product CHOH* is predicted to occupy the top site.[45,46] Thus, the reaction would have required the diffusion of COH* from the hollow site to the top site, yielding a high energy barrier (1.25 eV) on Cu(111). For this reason, it is energetically more favorable for COH* to be reduced into C* (and H_2O) on Cu(111) with a smaller barrier of 1.09 eV. However, in Co@Cu, thanks to the stronger bonding at the Co site due to its narrowed d-band, both COH* and CHOH* can be stabilized at the Co top site, which eliminates the need for diffusion and leads to a lower energy barrier (0.82 eV) for the reduction of COH* to CHOH*. As shown in the insets of Figure 4, the reduction of COH* to CHOH* (IS4 → TS4 → FS4) proceeds via the WS model in which a surface proton H1 is transferred directly to the C atom of COH*, assisted by the water molecule. The reduction of COH* to C* on Co@Cu, on the other hand, is highly endothermic (~1.10 eV), thus is unlikely to occur. Hence, we conclude that the deviation in the reaction pathway between Cu (COH* → C*) and Co@Cu (COH* → CHOH*) results from the strengthened bonding at Co due to its narrowed d-band, and this deviation eventually leads to different final products, CH_4 on Cu and CH_3OH on Co@Cu.

3.7. CHOH* → CH_2OH^* and CH_2OH^* → CH_3OH. The reduction of CHOH* to CH_2OH^* (IS5 → TS5 → FS5) and the reduction of CH_2OH^* to CH_3OH (IS6 → TS6 → FS6) proceed

DOI: 10.1021/acs.jpcc.8b12449
J. Phys. Chem. C XXXX, XXX, XXX−XXX

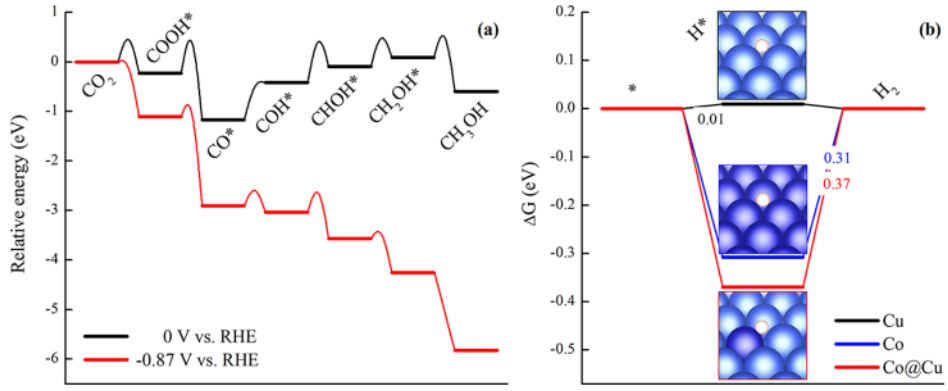

Figure 5. (a) Relative energy diagrams for CH_3OH production on Co@Cu at 0 and −0.87 V vs RHE. (b) Free energy diagrams for HER on Cu(111), Co(111), and Co@Cu surfaces at 0 V vs RHE. The adsorption geometries are shown in the insets. Blue, dark blue, and white spheres represent Cu, Co, and H atoms, respectively.

via the WS model, leading to the final product of CH_3OH on Co@Cu (Figure 4). These two steps have relatively low activation barriers (0.54 and 0.42 eV) compared to the hydrogenation of COH*. The energy barriers for these two steps are also lower than those of the branched pathways, that is, CHOH* → CH* + H_2O (0.98 eV) and CH_2OH^* → CH_2^* + H_2O (0.68 eV), which proceed via the HS model (Figures S6 and S7). Finally, the reduction of CH_3OH to CH_3^* (and H_2O) on Co@Cu is unlikely because of a high barrier of 1.74 eV (Figure S8).

It is reported that an icelike water bilayer structure on Cu(111) could aid the shuttling of protons and lower the energy barrier of O−H bond formation.[45,46] On the other hand, the bilayer structure has a negligible effect on the formation of the C−H bond which proceeds through a direct proton transfer.[45,46] In the preceding discussion, we have already examined the six branched pathways (CO_2 → HCOO*, COOH* → HCOOH, CO* → CHO*, COH* → C*, CHOH* → CH*, and CH_2OH^* → CH_2^*) in the presence of a water molecule per adsorbate, and they were found less favorable than the pathway of CH_3OH formation (CO_2 → COOH* → CO* → COH* → CHOH* → CH_2OH^* → CH_3OH). In the following, we re-examine these pathways by including more water molecules with the bilayer structure in the calculations. Because the first three branches proceed via the WS model, the bilayer water structure should have a negligible effect on them, thus these branches are not considered further. The COH* → C* branch takes place via the HS model, but it is highly endothermic, and thus it remains unfavorable and is not considered in the following calculations. Therefore, we only need to re-examine the last two branches, that is, CHOH* → CH* and CH_2OH^* → CH_2^*, which involve the shuttling of protons. More specifically, an icelike water bilayer is introduced on the surface in the computational model (Figures S6 and S7), similar to the previous works.[45,46] The activation barriers for these two pathways are estimated as 1.02 and 0.66 eV, which remain higher than those along the established pathway. Therefore, we conclude that the incorporation of additional solvation in the form of bilayer water molecules does not change the reaction mechanism on Co@Cu.

Figure 5a summarizes the potential-dependent free energy diagrams for CH_3OH production on Co@Cu. The reduction of COH* to CHOH* is identified as the overpotential-determining step. At the potential of −0.87 V versus RHE, all reaction steps are energetically downhill with energy barriers (≤0.4 eV) that are surmountable at room temperature. This overpotential is 24% less negative than the corresponding value (−1.15 V) on Cu(111) for the formation to CH_4.[45,46] We have also examined the HER, which is a key side reaction competing with CO_2RR.[5,6] In Figure 5b, we display the HER free energy diagram on Co@Cu in comparison with that on pure Cu and Co surfaces. We find that the pure Co surface bonds to H* more strongly than the pure Cu surface, consistent with previous work.[66,67] Interestingly, because of the narrowed d-band, the Co@Cu surface bonds to H* even more strongly than the pure Co surface, increasing the HER overpotential on Co@Cu. The calculated HER overpotential on Co@Cu is −0.37 V versus RHE, which is 0.06 and 0.36 V more negative than that on the pure Co and Cu surfaces. Thus, the addition of Co helps reduce HER on Cu, albeit only slightly.

4. CONCLUSIONS

In summary, we predict that Cu-based SAAs are capable of electrocatalyzing CO_2 into liquid fuel CH_3OH based on first-principles calculations. As one of the most promising candidates, Co@Cu, is shown to be selective toward the production of CH_3OH at a lower overpotential than that on Cu(111) for producing CH_4. The formation of the free atom-like d-band due to the isolated Co atoms is revealed to play a crucial role in CO_2RR by modulating the adsorption strengths on the Co@Cu surface. In particular, we show that the narrowed Co d-band is responsible for stabilizing b-CO_2 on the surface, which is essential to the initial hydrogenation steps. More importantly, we find that the narrowed Co d-band gives rise to stronger bonding between COH* and Co, which in turn eliminates the migration of the intermediate and lowers the activation energy for the hydrogenation of COH* to CHOH*. Finally, the isolated Co atoms are expected to reduce C−C coupling, leading to selective and efficient formation of CH_3OH. Our work offers an encouraging prospect of SAAs for CO_2RR and hopefully could inspire future experimental effort toward the discovery of superior metal catalysts for CO_2RR.

■ ASSOCIATED CONTENT

Supporting Information

The Supporting Information is available free of charge on the ACS Publications website at DOI: 10.1021/acs.jpcc.8b12449.

Energy barriers for Co atoms aggregating to form dimer and diffusing into the interior of Cu; free energy difference between different H_2O and CO_2 occupations on Co@Cu;

DOI: 10.1021/acs.jpcc.8b12449
J. Phys. Chem. C XXXX, XXX, XXX−XXX

relative energy diagrams for the reduction of b-CO_2 to HCOO*, COOH* to HCOOH, CHOH* to CH* and H_2O, CH_2OH* to CH_2^* and H_2O, CH_3OH to CH* and H_2O, b-CO_2 to COOH*, COOH* to CO* and H_2O, CO* to COH*, COH* to CHOH*, CHOH* to CH_2OH*, and CH_2OH* to CH_3OH on Co@Cu; parameters for determining potential-dependent barriers for CH_3OH production; and optimized geometries of the TSs (PDF)

AUTHOR INFORMATION

Corresponding Author

*E-mail: ganglu@csun.edu.

ORCID

Zhonglong Zhao: 0000-0002-2245-9045

Notes

The authors declare no competing financial interest.

ACKNOWLEDGMENTS

This work was supported by the National Science Foundation (DMR-1828019).

REFERENCES

(1) Lewis, N. S.; Nocera, D. G. Powering the Planet: Chemical Challenges in Solar Energy Utilization. *Proc. Natl. Acad. Sci. U.S.A.* **2006**, *103*, 15729−15735.

(2) Olah, G. A.; Prakash, G. K. S.; Goeppert, A. Anthropogenic Chemical Carbon Cycle for a Sustainable Future. *J. Am. Chem. Soc.* **2011**, *133*, 12881−12898.

(3) Jhong, H.-R. M.; Ma, S.; Kenis, P. J. A. Electrochemical Conversion of CO2 to Useful Chemicals: Current Status, Remaining Challenges, and Future Opportunities. *Curr. Opin. Chem. Eng.* **2013**, *2*, 191−199.

(4) Hori, Y.; Wakebe, H.; Tsukamoto, T.; Koga, O. Electrocatalytic Process of CO Selectivity in Electrochemical Reduction of CO2 at Metal Electrodes in Aqueous Media. *Electrochim. Acta* **1994**, *39*, 1833−1839.

(5) Kuhl, K. P.; Hatsukade, T.; Cave, E. R.; Abram, D. N.; Kibsgaard, J.; Jaramillo, T. F. Electrocatalytic Conversion of Carbon Dioxide to Methane and Methanol on Transition Metal Surfaces. *J. Am. Chem. Soc.* **2014**, *136*, 14107−14113.

(6) Peterson, A. A.; Abild-Pedersen, F.; Studt, F.; Rossmeisl, J.; Nørskov, J. K. How Copper Catalyzes the Electroreduction of Carbon Dioxide into Hydrocarbon Fuels. *Energy Environ. Sci.* **2010**, *3*, 1311−1315.

(7) Kuhl, K. P.; Cave, E. R.; Abram, D. N.; Jaramillo, T. F. New Insights into the Electrochemical Reduction of Carbon Dioxide on Metallic Copper Surfaces. *Energy Environ. Sci.* **2012**, *5*, 7050−7059.

(8) Peterson, A. A.; Nørskov, J. K. Activity Descriptors for CO2 Electroreduction to Methane on Transition-Metal Catalysts. *J. Phys. Chem. Lett.* **2012**, *3*, 251−258.

(9) Li, Y.; Sun, Q. Recent Advances in Breaking Scaling Relations for Effective Electrochemical Conversion of CO2. *Adv. Energy Mater.* **2016**, *6*, 1600463.

(10) Mistry, H.; Varela, A. S.; Kühl, S.; Strasser, P.; Cuenya, B. R. Nanostructured Electrocatalysts with Tunable Activity and Selectivity. *Nat. Rev. Mater.* **2016**, *1*, 16009.

(11) Chen, Z.; Zhang, X.; Lu, G. Overpotential for CO2 Electroreduction Lowered on Strained Penta-Twinned Cu Nanowires. *Chem. Sci.* **2015**, *6*, 6829−6835.

(12) Raciti, D.; Livi, K. J.; Wang, C. Highly Dense Cu Nanowires for Low-Overpotential CO2 Reduction. *Nano Lett.* **2015**, *15*, 6829−6835.

(13) Li, C. W.; Ciston, J.; Kanan, M. W. Electroreduction of Carbon Monoxide to Liquid Fuel on Oxide-Derived Nanocrystalline Copper. *Nature* **2014**, *508*, 504−507.

(14) Roberts, F. S.; Kuhl, K. P.; Nilsson, A. High Selectivity for Ethylene from Carbon Dioxide Reduction over Copper Nanocube Electrocatalysts. *Angew. Chem., Int. Ed.* **2015**, *127*, 5268−5271.

(15) Jeon, H. S.; Kunze, S.; Scholten, F.; Roldan Cuenya, B. Prism-Shaped Cu Nanocatalysts for Electrochemical CO2 Reduction to Ethylene. *ACS Catal.* **2018**, *8*, 531−535.

(16) Watanabe, M.; Shibata, M.; Kato, A.; Azuma, M.; Sakata, T. Design of Alloy Electrocatalysts for CO[sub 2] Reduction. *J. Electrochem. Soc.* **1991**, *138*, 3382−3389.

(17) Kim, D.; Resasco, J.; Yu, Y.; Asiri, A. M.; Yang, P. Synergistic Geometric and Electronic Effects for Electrochemical Reduction of Carbon Dioxide Using Gold−Copper Bimetallic Nanoparticles. *Nat. Commun.* **2014**, *5*, 4948.

(18) Clark, E. L.; Hahn, C.; Jaramillo, T. F.; Bell, A. T. Electrochemical CO2 Reduction over Compressively Strained CuAg Surface Alloys with Enhanced Multi-Carbon Oxygenate Selectivity. *J. Am. Chem. Soc.* **2017**, *139*, 15848−15857.

(19) Rasul, S.; Anjum, D. H.; Jedidi, A.; Minenkov, Y.; Cavallo, L.; Takanabe, K. A Highly Selective Copper-Indium Bimetallic Electrocatalyst for the Electrochemical Reduction of Aqueous CO2to CO. *Angew. Chem., Int. Ed.* **2015**, *54*, 2146−2150.

(20) Xu, Z.; Lai, E.; Shao-Horn, Y.; Hamad-Schifferli, K. Compositional Dependence of the Stability of AuCu Alloy Nanoparticles. *Chem. Commun.* **2012**, *48*, 5626−5628.

(21) Zhao, Z.; Lu, G. Computational Screening of Near-Surface Alloys for CO2 Electroreduction. *ACS Catal.* **2018**, *8*, 3885−3894.

(22) Ju, W.; Bagger, A.; Hao, G.-P.; Varela, A. S.; Sinev, I.; Bon, V.; Roldan Cuenya, B.; Kaskel, S.; Rossmeisl, J.; Strasser, P. Understanding Activity and Selectivity of Metal-Nitrogen-Doped Carbon Catalysts for Electrochemical Reduction of CO2. *Nat. Commun.* **2017**, *8*, 944.

(23) Wang, Y.; Chen, Z.; Han, P.; Du, Y.; Gu, Z.; Xu, X.; Zheng, G. Single-Atomic Cu with Multiple Oxygen Vacancies on Ceria for Electrocatalytic CO2 Reduction to CH4. *ACS Catal.* **2018**, *8*, 7113−7119.

(24) Yang, H. B.; Hung, S.-F.; Liu, S.; Yuan, K.; Miao, S.; Zhang, L.; Huang, X.; Wang, H.-Y.; Cai, W.; Chen, R.; et al. Atomically Dispersed Ni(i) as the Active Site for Electrochemical CO2 Reduction. *Nat. Energy* **2018**, *3*, 140−147.

(25) Zhu, G.; Li, Y.; Zhu, H.; Su, H.; Chan, S. H.; Sun, Q. Curvature-Dependent Selectivity of CO2 Electrocatalytic Reduction on Cobalt Porphyrin Nanotubes. *ACS Catal.* **2016**, *6*, 6294−6301.

(26) Liu, J. Catalysis by Supported Single Metal Atoms. *ACS Catal.* **2017**, *7*, 34−59.

(27) Kyriakou, G.; Boucher, M. B.; Jewell, A. D.; Lewis, E. A.; Lawton, T. J.; Baber, A. E.; Tierney, H. L.; Flytzani-Stephanopoulos, M.; Sykes, E. C. H. Isolated Metal Atom Geometries as a Strategy for Selective Heterogeneous Hydrogenations. *Science* **2012**, *335*, 1209−1212.

(28) Lucci, F. R.; Liu, J.; Marcinkowski, M. D.; Yang, M.; Allard, L. F.; Flytzani-Stephanopoulos, M.; Sykes, E. C. H. Selective Hydrogenation of 1,3-Butadiene on Platinum−Copper Alloys at the Single-Atom Limit. *Nat. Commun.* **2015**, *6*, 8550.

(29) Lucci, F. R.; Lawton, T. J.; Pronschinske, A.; Sykes, E. C. H. Atomic Scale Surface Structure of Pt/Cu(111) Surface Alloys. *J. Phys. Chem. C* **2014**, *118*, 3015−3022.

(30) Jirkovský, J. S.; Panas, I.; Ahlberg, E.; Halasa, M.; Romani, S.; Schiffrin, D. J. Single Atom Hot-Spots at Au-Pd Nanoalloys for Electrocatalytic H2O2Production. *J. Am. Chem. Soc.* **2011**, *133*, 19432−19441.

(31) Zhang, L.; Wang, A.; Miller, J. T.; Liu, X.; Yang, X.; Wang, W.; Li, L.; Huang, Y.; Mou, C.-Y.; Zhang, T. Efficient and Durable Au Alloyed Pd Single-Atom Catalyst for the Ullmann Reaction of Aryl Chlorides in Water. *ACS Catal.* **2014**, *4*, 1546−1553.

(32) Aich, P.; Wei, H.; Basan, B.; Kropf, A. J.; Schweitzer, N. M.; Marshall, C. L.; Miller, J. T.; Meyer, R. Single-Atom Alloy Pd-Ag Catalyst for Selective Hydrogenation of Acrolein. *J. Phys. Chem. C* **2015**, *119*, 18140−18148.

(33) Pei, G. X.; Liu, X. Y.; Wang, A.; Lee, A. F.; Isaacs, M. A.; Li, L.; Pan, X.; Yang, X.; Wang, X.; Tai, Z.; et al. Ag Alloyed Pd Single-Atom

DOI: 10.1021/acs.jpcc.8b12449
J. Phys. Chem. C XXXX, XXX, XXX−XXX

Catalysts for Efficient Selective Hydrogenation of Acetylene to Ethylene in Excess Ethylene. *ACS Catal.* **2015**, *5*, 3717−3725.
(34) Li, Z.; He, T.; Matsumura, D.; Miao, S.; Wu, A.; Liu, L.; Wu, G.; Chen, P. Atomically Dispersed Pt on the Surface of Ni Particles: Synthesis and Catalytic Function in Hydrogen Generation from Aqueous Ammonia-Borane. *ACS Catal.* **2017**, *7*, 6762−6769.
(35) Qin, R.; Liu, P.; Fu, G.; Zheng, N. Strategies for Stabilizing Atomically Dispersed Metal Catalysts. *Small* **2018**, *2*, 1700286.
(36) Wang, Z.-T.; Darby, M. T.; Therrien, A. J.; El-Soda, M.; Michaelides, A.; Stamatakis, M.; Sykes, E. C. H. Preparation, Structure, and Surface Chemistry of Ni-Au Single Atom Alloys. *J. Phys. Chem. C* **2016**, *120*, 13574−13580.
(37) Baber, A. E.; Tierney, H. L.; Lawton, T. J.; Sykes, E. C. H. An Atomic-Scale View of Palladium Alloys and Their Ability to Dissociate Molecular Hydrogen. *ChemCatChem* **2011**, *3*, 607−614.
(38) Tierney, H. L.; Baber, A. E.; Sykes, E. C. H. Atomic-Scale Imaging and Electronic Structure Determination of Catalytic Sites on Pd/Cu Near Surface Alloys. *J. Phys. Chem. C* **2009**, *113*, 7246−7250.
(39) Tierney, H. L.; Baber, A. E.; Kitchin, J. R.; Sykes, E. C. H. Hydrogen Dissociation and Spillover on Individual Isolated Palladium Atoms. *Phys. Rev. Lett.* **2009**, *103*, 246102.
(40) Cheng, M.-J.; Clark, E. L.; Pham, H. H.; Bell, A. T.; Head-Gordon, M. Quantum Mechanical Screening of Single-Atom Bimetallic Alloys for the Selective Reduction of CO2 to C1 Hydrocarbons. *ACS Catal.* **2016**, *6*, 7769−7777.
(41) Inderwildi, O. R.; Jenkins, S. J.; King, D. A. When adding an unreactive metal enhances catalytic activity: NOx decomposition over silver-rhodium bimetallic surfaces. *Surf. Sci.* **2007**, *601*, L103−L108.
(42) Greiner, M. T.; Jones, T. E.; Beeg, S.; Zwiener, L.; Scherzer, M.; Girgsdies, F.; Piccinin, S.; Armbrüster, M.; Knop-Gericke, A.; Schlögl, R. Free-Atom-Like d States in Single-Atom Alloy Catalysts. *Nat. Chem.* **2018**, *10*, 1008−1015.
(43) Li, N.; Chen, X.; Ong, W.-J.; MacFarlane, D. R.; Zhao, X.; Cheetham, A. K.; Sun, C. Understanding of Electrochemical Mechanisms for CO2 Capture and Conversion into Hydrocarbon Fuels in Transition-Metal Carbides (MXenes). *ACS Nano* **2017**, *11*, 10825−10833.
(44) Favaro, M.; Xiao, H.; Cheng, T.; Goddard, W. A.; Yano, J.; Crumlin, E. J. Subsurface Oxide Plays a Critical Role in CO2 Activation by Cu (111) Surfaces to Form Chemisorbed CO2, The First Step in Reduction of CO2. *Proc. Natl. Acad. Sci. U.S.A.* **2017**, *114*, 6706−6711.
(45) Nie, X.; Esopi, M. R.; Janik, M. J.; Asthagiri, A. Selectivity of CO2Reduction on Copper Electrodes: The Role of the Kinetics of Elementary Steps. *Angew. Chem., Int. Ed.* **2013**, *52*, 2459−2462.
(46) Nie, X.; Luo, W.; Janik, M. J.; Asthagiri, A. Reaction Mechanisms of CO2 Electrochemical Reduction on Cu(111) Determined with Density Functional Theory. *J. Catal.* **2014**, *312*, 108−122.
(47) Ding, X.; De Rogatis, L.; Vesselli, E.; Baraldi, A.; Comelli, G.; Rosei, R.; Savio, L.; Vattuone, L.; Rocca, M.; Fornasiero, P.; et al. Interaction of Carbon Dioxide with Ni(110): A Combined Experimental and Theoretical Study. *Phys. Rev. B: Condens. Matter Mater. Phys.* **2007**, *76*, 195425.
(48) Liu, X.; Sun, L.; Deng, W.-Q. Theoretical Investigation of CO2 Adsorption and Dissociation on Low Index Surfaces of Transition Metals. *J. Phys. Chem. C* **2018**, *122*, 8306−8314.
(49) Ruban, A.; Hammer, B.; Stoltze, P.; Skriver, H. L.; Nørskov, J. K. Surface electronic structure and reactivity of transition and noble metals1Communication presented at the First Francqui Colloquium, Brussels, 19-20 February 1996.1. *J. Mol. Catal. A: Chem.* **1997**, *115*, 421−429.
(50) Darby, M. T.; Réocreux, R.; Sykes, E. C. H.; Michaelides, A.; Stamatakis, M. Elucidating the Stability and Reactivity of Surface Intermediates on Single-Atom Alloy Catalysts. *ACS Catal.* **2018**, *8*, 5038−5050.
(51) Kresse, G.; Furthmüller, J. Efficient iterative schemes forab initiototal-energy calculations using a plane-wave basis set. *Phys. Rev. B: Condens. Matter Mater. Phys.* **1996**, *54*, 11169−11186.
(52) Perdew, J. P.; Burke, K.; Ernzerhof, M. Generalized Gradient Approximation Made Simple. *Phys. Rev. Lett.* **1996**, *77*, 3865−3868.
(53) Grimme, S.; Antony, J.; Ehrlich, S.; Krieg, H. A Consistent and Accurate Ab Initio Parametrization of Density Functional Dispersion Correction (DFT-D) for the 94 Elements H-Pu. *J. Chem. Phys.* **2010**, *132*, 154104.
(54) Heyd, J.; Scuseria, G. E.; Ernzerhof, M. Hybrid Functionals Based on a Screened Coulomb Potential. *J. Chem. Phys.* **2003**, *118*, 8207−8215.
(55) Heyd, J.; Scuseria, G. E. Efficient hybrid density functional calculations in solids: Assessment of the Heyd-Scuseria-Ernzerhof screened Coulomb hybrid functional. *J. Chem. Phys.* **2004**, *121*, 1187−1192.
(56) Heyd, J.; Scuseria, G. E.; Ernzerhof, M. Erratum: "Hybrid functionals based on a screened Coulomb potential" [J. Chem. Phys. 118, 8207 (2003)]. *J. Chem. Phys.* **2006**, *124*, 219906.
(57) Monkhorst, H. J.; Pack, J. D. Special Points for Brillouin-Zone Integrations. *Phys. Rev. B: Solid State* **1976**, *13*, 5188−5192.
(58) Henkelman, G.; Jónsson, H. Improved Tangent Estimate in the Nudged Elastic Band Method for Finding Minimum Energy Paths and Saddle Points. *J. Chem. Phys.* **2000**, *113*, 9978−9985.
(59) Nørskov, J. K.; Rossmeisl, J.; Logadottir, A.; Lindqvist, L.; Kitchin, J. R.; Bligaard, T.; Jónsson, H. Origin of the Overpotential for Oxygen Reduction at a Fuel-Cell Cathode. *J. Phys. Chem. B* **2004**, *108*, 17886−17892.
(60) Cramer, C. J. *Essentials of Computational Chemistry: Theories and Models*, 2nd ed.; Wiley & Sons: Chichester, U.K., 2004.
(61) Luo, W.; Nie, X.; Janik, M. J.; Asthagiri, A. Facet Dependence of CO2 Reduction Paths on Cu Electrodes. *ACS Catal.* **2016**, *6*, 219−229.
(62) Nouvertné, F.; May, U.; Bamming, M.; Rampe, A.; Korte, U.; Güntherodt, G.; Pentcheva, R.; Scheffler, M. Atomic Exchange Processes and Bimodal Initial Growth of Co/Cu(001). *Phys. Rev. B: Condens. Matter Mater. Phys.* **1999**, *60*, 14382−14386.
(63) van Gastel, R.; Van Moere, R.; Zandvliet, H. J. W.; Poelsema, B. Vacancy-Mediated Diffusion of Co Atoms Embedded in Cu(001). *Surf. Sci.* **2011**, *605*, 1956−1961.
(64) Akhade, S. A.; Luo, W.; Nie, X.; Asthagiri, A.; Janik, M. J. Theoretical Insight on Reactivity Trends in CO2 Electroreduction across Transition Metals. *Catal. Sci. Technol.* **2016**, *6*, 1042−1053.
(65) Hammer, B.; Hansen, L. B.; Nørskov, J. K. Improved Adsorption Energetics within Density-Functional Theory using Revised Perdew-Burke-Ernzerhof Functionals. *Phys. Rev. B: Condens. Matter Mater. Phys.* **1999**, *59*, 7413−7421.
(66) Nørskov, J. K.; Bligaard, T.; Logadottir, A.; Kitchin, J. R.; Chen, J. G.; Pandelov, S.; Stimming, U. Trends in the Exchange Current for Hydrogen Evolution. *J. Electrochem. Soc.* **2005**, *152*, J23−J26.
(67) Sheng, W.; Myint, M.; Chen, J. G.; Yan, Y. Correlating the Hydrogen Evolution Reaction Activity in Alkaline Electrolytes with the Hydrogen Binding Energy on Monometallic Surfaces. *Energy Environ. Sci.* **2013**, *6*, 1509−1512.

DOI: 10.1021/acs.jpcc.8b12449
J. Phys. Chem. C XXXX, XXX, XXX−XXX